Supporting information (SI) Appendix for

Decoding Cortical Activity through Neuronal Tracing Connectome-Harmonics in Marmosets

Running title: Cellular-functional dependency in marmosets

Jie XIA[1,2], Cirong LIU[3], Jiao LI[1,2], Yao MENG[1,2], Siqi YANG[4], Huafu CHEN[1,2]✉, Wei LIAO[1,2]✉

[1] The Clinical Hospital of Chengdu Brain Science Institute, School of Life Science and Technology, University of Electronic Science and Technology of China, Chengdu 611731, P.R. China.

[2] MOE Key Lab for Neuroinformation, High-Field Magnetic Resonance Brain Imaging Key Laboratory of Sichuan Province, University of Electronic Science and Technology of China, Chengdu 611731, P.R. China.

[3] Institute of Neuroscience, CAS Key Laboratory of Primate Neurobiology, Center for Excellence in Brain Science and Intelligence Technology, Chinese Academy of Sciences, Shanghai 200031, P.R. China.

[4] School of Cybersecurity, Chengdu University of Information Technology, Chengdu 610225, P.R. China

✉ Corresponding authors:

Huafu CHEN (chenhf@uestc.edu.cn), and Wei LIAO (weiliao.wl@gmail.com).

The Clinical Hospital of Chengdu Brain Science Institute, MOE Key Laboratory for Neuroinformation, University of Electronic Science and Technology of China, Chengdu 610054, P.R. China. Fax: +86-28-61831273. Tel: +86-28-61831273.

Supplementary Materials and Methods

SI-1 Resting-state fMRI data in the awake marmosets

1.1 Data acquisition

Seven marmosets (all male) from the National Institutes of Health (NIH) cohort were scanned in a 7T/30 cm horizontal MRI[1,2]. They were acquired with a 2D gradient echo planar imaging (EPI) sequence (TR = 2000 ms, TE = 22.2 ms, flip angle = 70.4°, FOV = 28×36 mm, matrix size = 56×72, 38 axis slices, resolution = 0.5 mm isotropic, 512 time points, each run is 17 min long). Two sets of spin-echo EPI with opposite phase-encoding directions (LR and RL) were also collected for EPI-distortion correction (TR = 3000 ms, TE = 36 ms, flip angle = 90°, FOV = 28 × 36 mm, matrix size = 56 × 72, 38 axial slices, slice thickness = 0.5 mm, eight volumes for each set). After the fMRI session, a T2-weighted structural scan was acquired (TR = 6000 ms, TE = 9 ms, flip angle = 90°, FOV = 28 × 36 mm, matrix size = 112 × 144, 38 axis slices, resolution = 0.25 × 0.25 × 0.5 mm3, number of averages = 8)[1,2].

1.2 MRI data preprocessing

All fMRI data were preprocessed using Analysis of Functional NeuroImages (AFNI)[3] and FMRIB Software Library (FSL) [4], which included slice-timing correction, motion correction, spatial smoothing, confound signal regressed, and band-pass filtered. For the fMRI data with opposing phase encodings, EPI-distortion was corrected (FSL's *topup*). Then, each fMRI run was registered to its T2-weighted image using rigid-body transformation. The T2-weighted images were then nonlinearly transformed to the Paxinos atlas[5,6], and the resulting transformation matrices were saved and used for

functional image registration. Images were smoothed using a 1 mm full-width at half-maximum (FWHM) Gaussian kernel to reduce noise (AFNI's *3dmerge*). Several regression covariates were considered to remove potential noise and motion effects (AFNI's *3dDeconvolve*), including demeaned and derivatives of motion parameters, motion-censor regressors, white matter, and cerebrospinal fluid signal. Finally, the pre-processed time courses were band-pass filtering corresponding to the frequency range 0.01 to 0.1 Hz.

SI-2 Graph signal processing on the marmoset data

2.1 Connectome Laplacian of the cellular connectome

A random walk defined on a directed weighted graph $\mathcal{G} = (V, E, A)$ is a homogeneous Markov chain $\chi = (X_n)_{n\geq 0}$, which is not necessarily invertible in a finite state space. Its transition probability is proportional to the weight of the edge[7]. The random walk is defined by a transition probability matrix P, where $P(i,j)$ denotes the probability of walking from node *i* to node *j*. Since the entries of $P(i,j)$ are probabilities, it follows that $P(i,j) \geq 0$, and $\sum_{j\in V} P(i,j) = 1, \forall\ \ i,j \in V$. Therefore, for a directed graph $\mathcal{G} = (V, E, A)$ with edge weights $A = \{A_{ij}\}_{1\leq i,j\leq N} \in R_+^{N\times N}$ defined as the FLNe value of tracer-based cellular connectome (CC) in the marmosets, P can be defined as,$P(i,j) = \frac{A_{ij}}{\sum_j A_{ij}}$. From the point of view of graph theory, the transition matrix $P \in R^{N\times N}$ is equal to

$$P = D^{-1}A, \qquad (1)$$

where $D = D_{ii} = \sum_{j=1}^{N} A_{ij}$, denotes the out-degrees matrix of the directed graph.

If the random walk χ with transition matrix P is ergodic (irreducible and aperiodic), then it has a unique stationary distribution π, i.e. $\pi P=\pi$, with $\sum_{i=1}^{N}\pi(v_i)=1, \pi(v_i)\geq 0$[7,8]. The normalized Laplacian of a directed graph $\mathcal{G}$[7,8] is defined by,

$$\mathcal{L} = I - \frac{\Pi^{1/2}P\Pi^{-1/2}+\Pi^{-1/2}P*\Pi^{1/2}}{2}, \quad (2)$$

where $\Pi = diag\{\pi(v_1),\cdots,\pi(v_N)\}$ is the diagonal matrix of the stationary distribution, I is the identity matrix, and P^* stands for the conjugated transpose of P.

2.2 Generation of graph surrogate signals

We generated two types of surrogate functional signals by spectral randomization. The first, we generated random graphs using the Brain Connectivity Toolbox (https://sites.google.com/site/bctnet/) [9]. This shuffles the connections of the original connection matrix while preserving its degree distribution[10]. Then functional signals were projected onto harmonics of random graphs to reconstruct surrogate activity pattern.

The second, we generate surrogate functional signals based on the empirical CC matrix ***A*** using graph phase randomization[11,12]. The graph spectral coefficients are randomized by randomly flipping the signs and used to reconstruct the surrogate functional signal $f_{it}^{(null)}$. The random sign flips are stored on the diagonal of Φ_{graph}. The empirical cellular connectome harmonics are replaced by spectral randomization $\Psi\Phi_{graph}$ to generate the surrogate signals,

$$f_{it}^{(null)} = \Psi\Phi_{graph}\Psi^T f_i^t \quad (3)$$

Graph phase randomization produces surrogate graph signals where the smoothness in space remains maintained, but non-stationary spatial effects are

destroyed. Same permutation time series matrix across time keeps temporal correlation properties and preserves power spectral density[12].

SI-3 Connectivity embedding

We used diffusion embedding[13] to project a set of embeddings into a lower-dimensional space. Briefly, we used the top 10% connections of each row of CC and FC matrix to compute non-negative symmetric affinity matrices that capture the similarity between features in cortical areas. Diffusion map embedding was used to estimate low-dimensional representations of affinity matrices. This algorithm was controlled by two parameters α and t, we followed the previous recommendation[13-15] and set $\alpha = 0.5$ and $t = 0$, a setting that preserved the global relationship between data points in the embedding space.

SI-4 Null models of spatial correlations

The intrinsic spatial smoothing of two given cortical maps may exaggerate the significance of their spatial correlation. To this end, we used two categories of null models: spatial auto-correlation preserving permutation tests (*spin* tests)[16,17] and Moran spectral randomization (MSR)[18]. The spin test assesses the statistical significance of correlations across brain areas. Specifically, cortical parcels' spatial coordinates were randomly rotated to generate a null model, and original parcels were reassigned parcel values based on the closest resulting parcel (10,000 repetitions). The procedure was performed only for the left hemisphere. Then, we computed the

percentile rank of the actual correlation in the random correlations. The spherical permutation P_{spin} values were obtained by comparison to the null models (<2.5th, or >97.5th percentile).

The MSR method[18] generated normally distributed null models with similar spatial auto-correlations for irregularly spaced data. Thus, we computed the randomized data using MSR and the singleton procedure[18]. Then, to find a P_{Moran}, we calculated the percentile rank between the actual data and the 10,000 randomized data. We considered the correlation significant if it is lower or higher than the 2.5th/97.5th percentile, respectively. In addition, to improve the standards correlation analysis, we identified outliers bootstrapping the Mahalanobis distance D_s from the bivariate mean, and excluded outliers with a mean D_s of six or greater[19].

Supplementary Result

The neuronal tracing connectome informs cortical activity and connectivity

To evaluate the functionally meaningful of CC harmonics in capturing spontaneous brain activity in the marmosets, we first generated 1000 directed random graphs that preserve the same node strengths of the CC graph. Furthermore, we compared the ability of CC and directed random graphs to capture the energy of human resting-state functional activity. We found that the number of connected harmonics required to capture 80% of functional activity energy in all random graphs exceeds the empirical CC graph (*Figure S8*), suggesting CC harmonics as a canonical basis provided a sparse representation of brain activity.

The empirical functional connectivity (FC) matrix (55 × 55 areas) derived from BOLD-fMRI at rest showed modular network organization (*Figure S9A*, left panel, and *Figure S10A*). One consists of the frontal, lateral, and inferior temporal cortex, while the other mainly contains motor, premotor, somatosensory, and visual areas. Globally, the pattern of nodal strength of empirical FC is positively corrected with nodal strength of CC ($\rho = 0.57$, $P_{spin} < 0.001$) (*Figure S9A*, right panel).

To further evaluate how the CC informs FC, we replaced empirical CC harmonics with spectral randomization to obtain surrogate FC (CC-informed surrogate FC), which incorporated CC architecture knowledge. The surrogated FC also showed modular network organization (*Figure S9B*, right panel, and *Figure S10B*), while CC-informed surrogates FC patterns contrasted more than empirical FC (*Figure S10*). The pattern of nodal strength of surrogated FC is positively corrected with nodal strength of CC by a judicious random walk ($\rho = 0.77$, $P_{spin} < 0.001$) (*Figure S9B*, right panel). Interestingly, the Spearman correlation of nodal strengths between CC driven by random walk

operator and surrogate FC (*Figure S9B*, right panel) was significantly higher than the correlation between CC and empirical FC (Z = 2.004, $P < 0.05$, comparison of two correlation coefficients from dependent samples https://www.psychometrica.de/korrelation.html). This result suggests the spatial map of rs-fMRI activity emerges from specific sign combination of CC harmonics. Above all, cortical connectivity results of the complex interplay of the CC harmonics in the marmosets.

Supplementary Figures

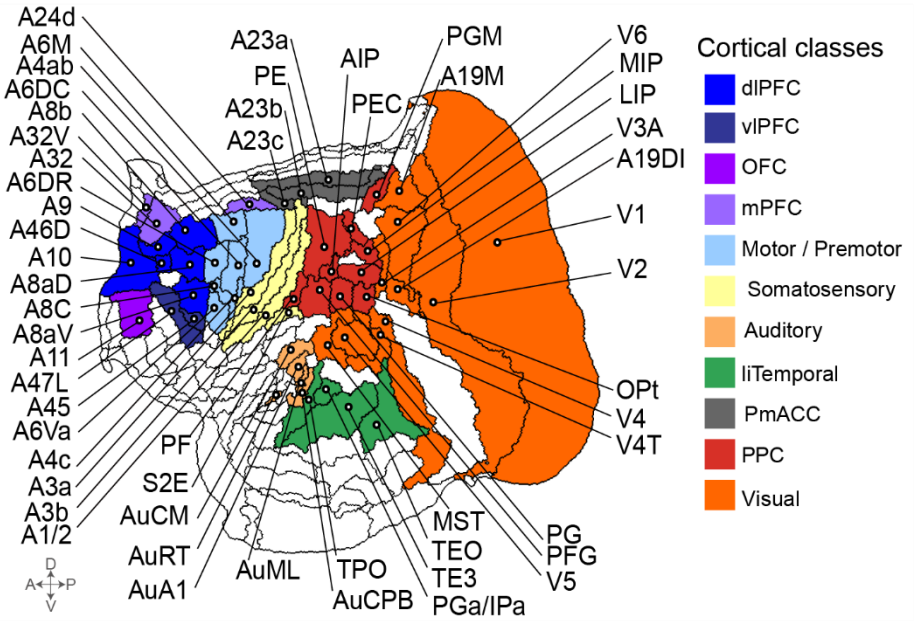

Figure S1. **The flat map of the marmoset.** The analysis focuses on 55 cortical areas marked with different colors on a two-dimensional flat map of the marmoset cortex according to the different cortical classes[5,20,21]. The white-shaded areas were those for which no tracer was injected. For abbreviations of the brain areas, see *Table S1*.

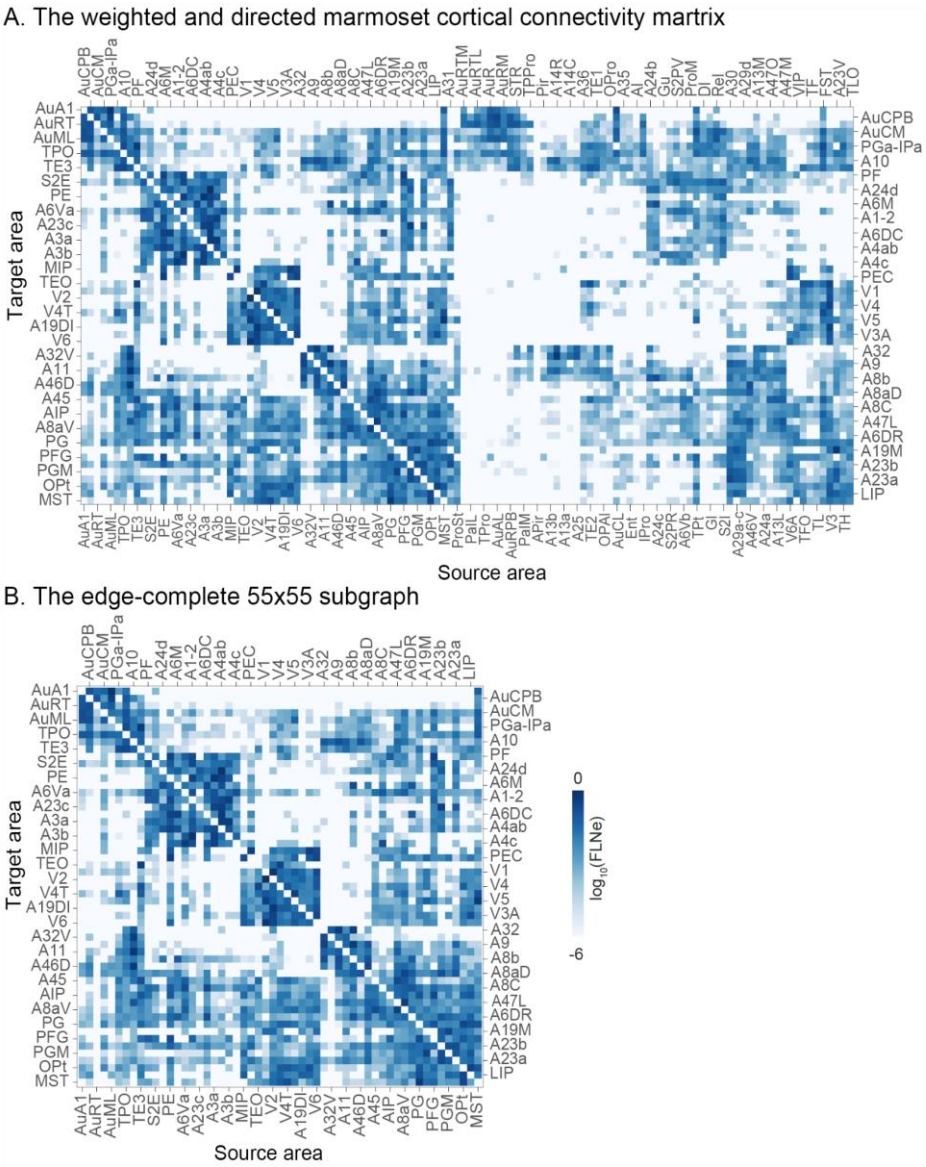

Figure S2. **Weighted connectivity matrix**. **(A)** The weighted and directed marmoset cortical interareal connectivity matrix. The rows were the 55 target areas, and the columns were the 116 source areas that provided inputs to the target areas. Each entry in the matrix was the base 10 logarithm of the arithmetic mean of the (log_{10}(FLNe)) across injections within the same target area. Darker shades of color represented stronger connection weights, white represented no connection. **(B)** The edge-complete subgraph, in which all inputs and outputs were known, showed a dense matrix of topological connections.

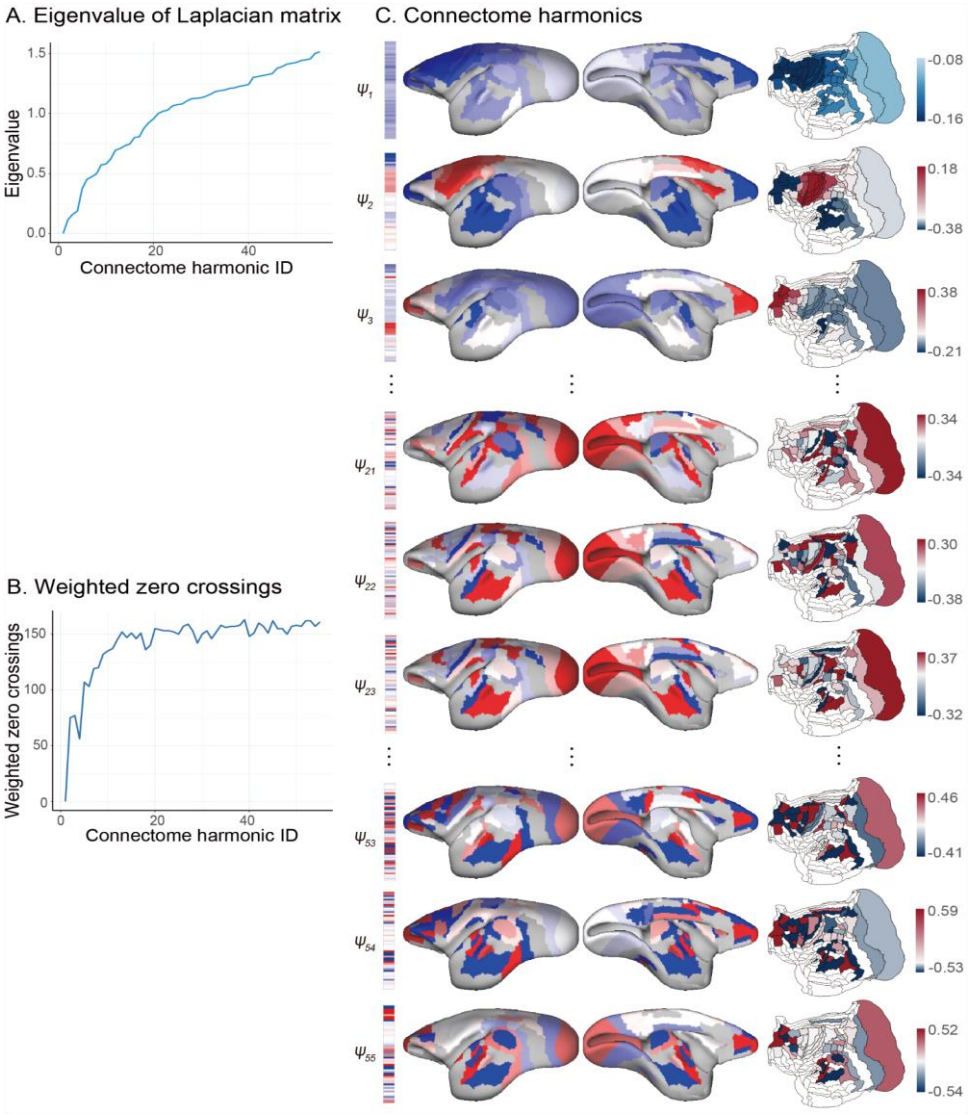

Figure S3. **Connectome harmonics are given by the eigenvectors of the graph Laplacian of the marmoset connectome. (A)** The eigenvalues of the Laplace matrix. **(B)** The number of weighted zero crossings along the graph structure for each connectome harmonic. The Laplacian eigenvectors associated with larger eigenvalues cross zero more often, suggesting the increasing complexity of harmonic modes with higher spatial frequency. **(C)** Several cellular connectome harmonics used two equivalent representations: one was a color-coded eigenvector, where each element corresponded to a brain area; the other was a projection of the eigenvector onto the brain surface or flat map. Negative–zero–positive values were colored as blue–white–red. We showed the three harmonics corresponding to the three smallest graph Laplacian eigenvalues (low

frequency harmonics), the three harmonics corresponding to the middle of eigenvalues (intermediate frequency harmonics), and the three harmonics (high frequency harmonics) corresponding to the three largest eigenvalues.

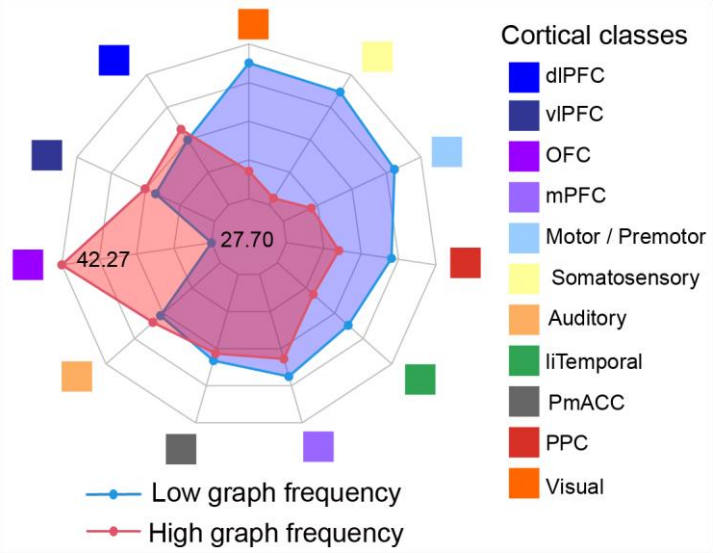

Figure S4. Cortical-level energy concentrations of low and high graph frequency signal comparisons.

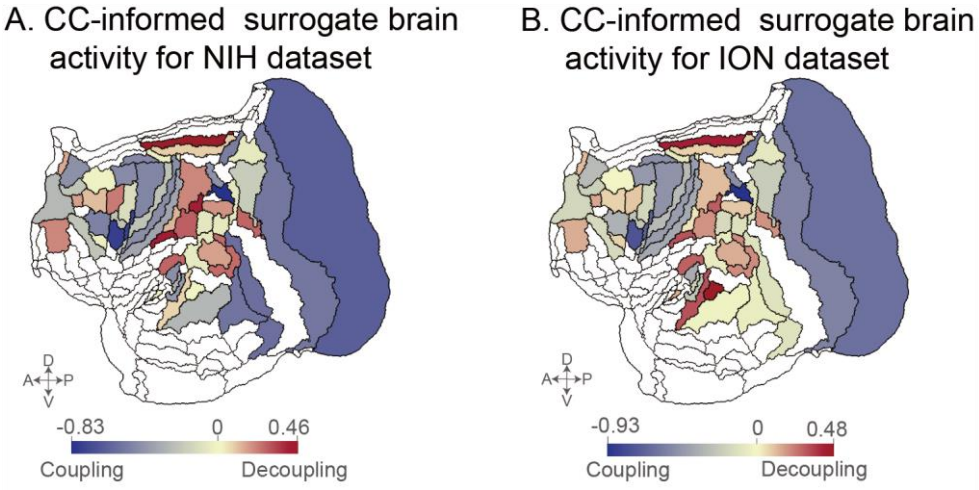

Figure S5. The cellular-function dependency (CFD) pattern of surrogate brain activity with knowledge of the underlying cellular connectome. Observed activation patterns emerge with specific combinations of neuronal tracing connectome harmonics, which are randomized in surrogate brain activity. The surrogates brain activity generates a null distribution of the CFD index, thus allowing detect significant CFD strength in empirical functional activity.

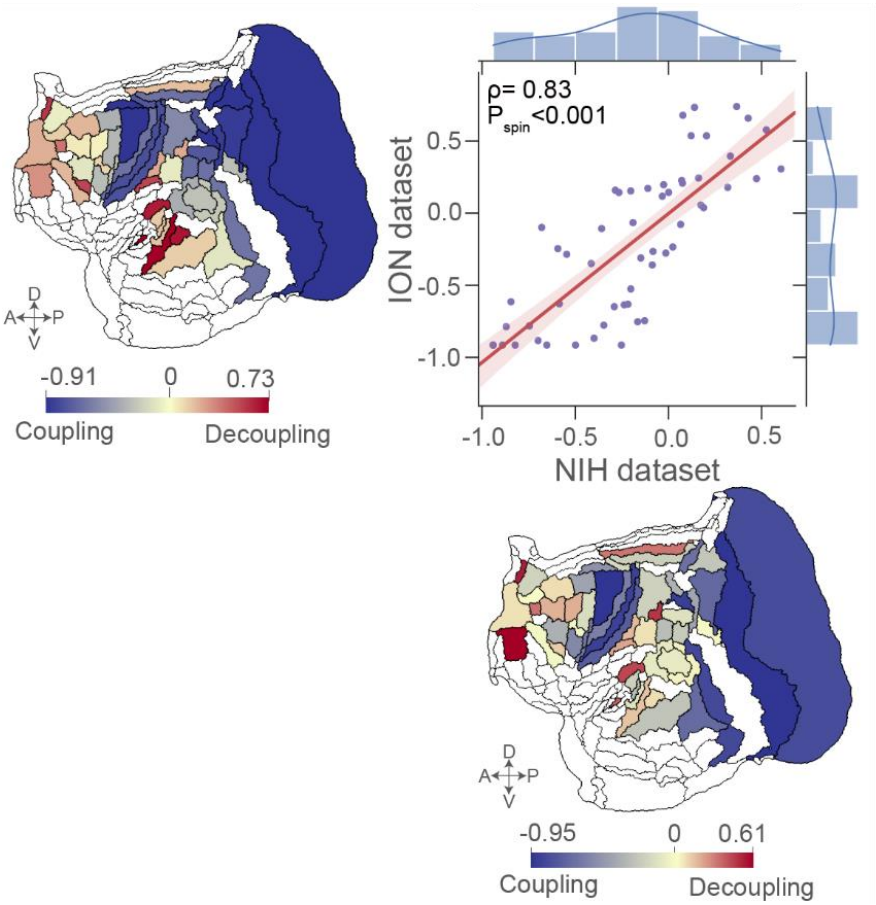

Figure S6. The spatial correlation between the National Institutes of Health (NIH) sites dataset and the Institute of Neuroscience (ION) sites dataset showed excellent reproducibility. Correlation significance (P_{spin}) was assessed using a spin test that preserved the spatial autocorrelation.

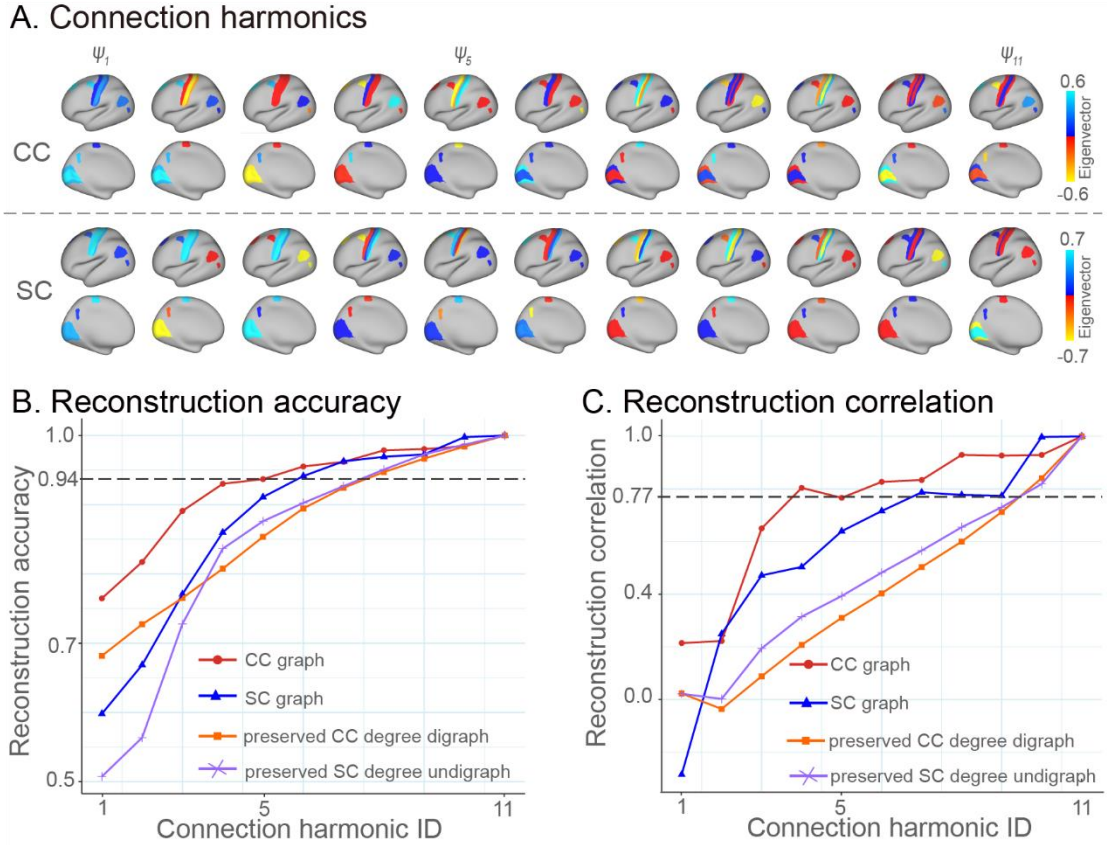

Figure S7. **Reconstruction accuracy of human resting-state functional activity and connectivity as a function of the number of harmonic modes. (A)**The tracer-based cellular connectivity (CC) and dMRI-based structural connectivity (SC) harmonic modes. **(B)** Reconstruction accuracy of resting-state functional activity across 11 common homologous areas. The energy ratio between empirical and reconstructed cortical activity quantified the reconstruction accuracy. **(C)** The Pearson correlation between empirical and reconstructed FC across 55 edges. The empirical intrinsic activity and FC were obtained from resting-state BOLD-fMRI in the human brain. The reconstructed human cortical activity and FC were achieved using the marmoset's CC harmonics, human SC harmonics, and two null model graphs. We generated 1000 directed random graphs or undigraph that preserve the same node degree of the connectivity matrix.

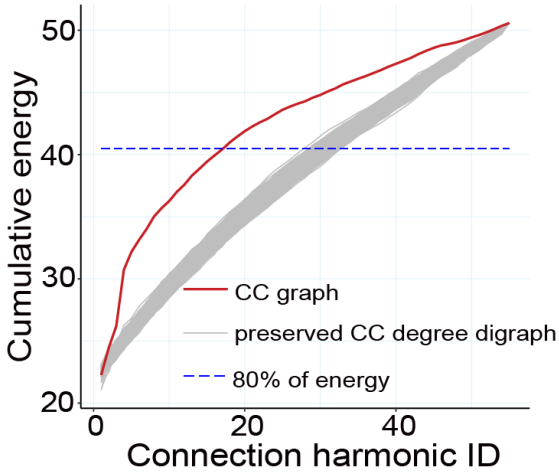

Figure S8. **Comparison of the ability of CC and directed random graphs to capture the energy of human resting-state functional activity.** For the CC graph (red line) and 1000 directed random graphs (grey line), the accumulated energy with more connection harmonics are added. The blue dashed line represents 80% of the total energy.

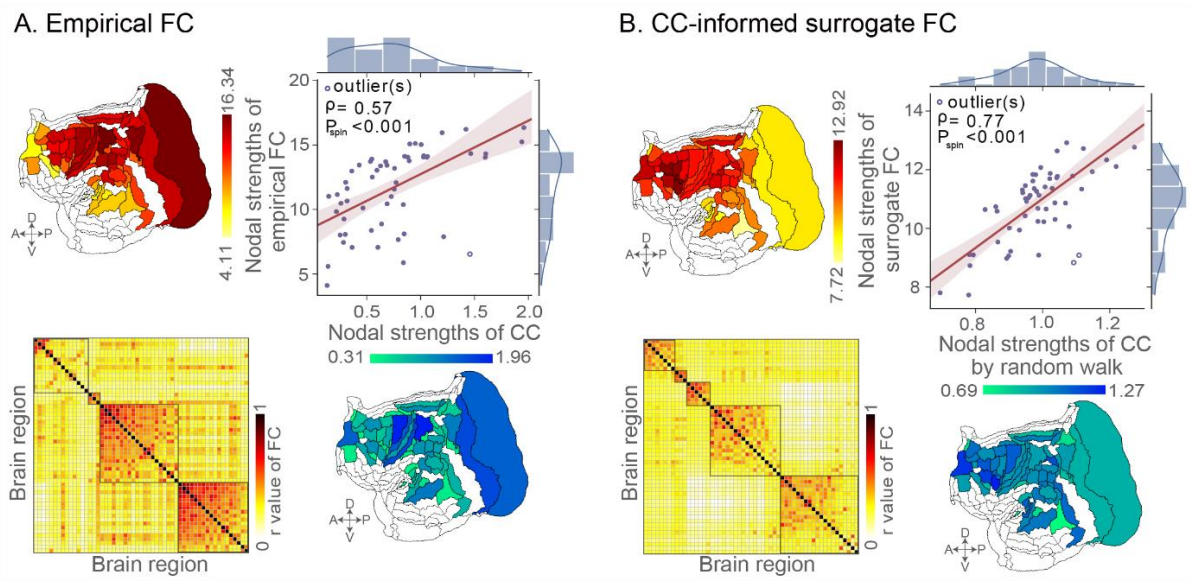

Figure S9. Functional connectivity (FC) informed by cellular connectome in the marmosets. **(A)** The pairwise Pearson correlation of empirical BOLD-fMRI signals obtained empirical FC matrix. The nodal strength of empirical CC was positively correlated with empirical FC (ρ = 0.57, P_{spin} < 0.001). **(B)** CC-informed surrogate FC matrix and surrogate functional signals with CC knowledge were generated using spectral coefficient randomization. The nodal strength of CC was positively correlated with that of surrogate FC matrix (ρ = 0.77, P_{spin} < 0.001). P_{spin} was evaluated using 10,000 spin tests that preserved spatial autocorrelation. Filled circles denoted data were included in the correlation, while open circles represented outliers.

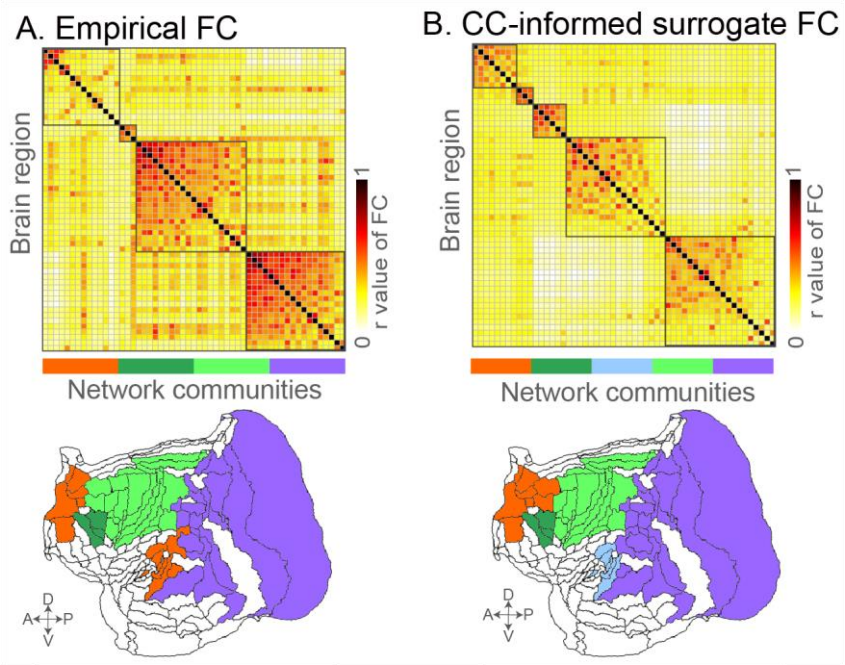

Figure S10. The modular organization of functional connectivity (FC). A greedy Louvain-like algorithm was used to identify network communities. **(A)** Empirical FC matrix revealed four communities. **(B)** Cellular connectome (CC)-informed surrogate FC matrix revealed five communities. Top row: adjacency matrix reordered by community assignment and correlation coefficient (r). Bottom row: flat map projections of community assignments.

Supplementary Tables

Table S1. Abbreviations of the names of cortical areas grouped in the major cortical subdivisions.

Abbreviation	Full name
Dorsolateral prefrontal cortex (dlPFC)	
A10	Area 10
A9	Area 9
A8b	Area 8b
A46D	Area 46, dorsal part
A8aD	Area 8a, dorsal part
A8aV	Area 8a, ventral part
Ventrolateral prefrontal cortex (vlPFC)	
A45	Area 45
A47L	Area 47 (12), lateral part
Orbito frontal cortex	
A11	Area 11
Medial prefrontal cortex	
A24d	Area 24d
A32	Area 32
A32V	Area 32, ventral part
Motor and premotor cortex	
A6M	Area 6, medial (supplementary motor) part
A6Va	Area 6, ventral, part a
A6DC	Area 6, dorsocaudal part
A4ab	Area 4, parts a and b (primary motor, representation of axial and limb musculature)
A4c	Area 4, part c (primary motor, representation of head musculature)
A8C	Area 8, caudal part
A6DR	Area 6, dorsorostral part
Somatosensory cortex	
S2E	Secondary somatosensory area, external part
A1-2	Areas 1 and 2

A3a	Area 3a
A3b	Area 3b (primary somatosensory area)
Auditory cortex	
AuA1	Primary auditory area
AuCPB	Caudal parabelt area
AuRT	Rostrotemporal area
AuCM	Caudomedial area
AuML	Middle lateral area
Lateral and inferior temporal cortex (litemporal)	
PGa-IPa	Areas PGa and IPa (fundus of superior temporal ventral area)
TPO	Temporo-parieto-occipital association area
TE3	Temporal area TE, part 3
TEO	Temporal area TE, occipital transition part
Posterior cingulate,medial,and retrosplenial cortex (PmACC)	
A23c	Area 23c
A23b	Area 23b
A23a	Area 23a
Posterior parietal cortex (PCC)	
PF	Parietal area PF
PE	Parietal area PE
MIP	Medial intraparietal area
PEC	Parietal area PE, caudal transitional part
AIP	Anterior intraparietal area
PG	Parietal area PG
PFG	Parietal area PFG
PGM	Parietal area PG, medial part
OPt	Occipito-parietal transitional area
LIP	Lateral intraparietal area
Visual cortex	
V1	Primary visual area
V2	Visual area 2
V4	Visual area 4 (ventrolatereral anterior area, VLA)
V4T	Visual area 4, transitional part (middle temporal crescent)

V5	Visual area 5 (middle temporal area, MT)
A19DI	Area 19, dorsointermediate part (DI)
V3A	Visual area 3a (dorsoanterior area, DA)
V6	Visual area 6 (dorsomedial area, DM)
A19M	Area 19, medial part
MST	Medial superior temporal area

Table S2. Details of homologous landmarks between human and marmoset[22]

#	Homologous area label	Label name in HCP-MMP1 atlases[23]	Label name in Paxinos atlases[5,6]	References
1	V1	V1	V1	Solomon and Rosa[24]
2	V2	V2	V2	Solomon and Rosa[24]
3	4	4	A4ab	Kaas[25]
4	3a	3a	A3a	Kaas[25]
5	3b	3b	A3b	Kaas[25]
6	1	1	A1-2	Kaas[25]
7	FEF	FEF	A8aV	Solomon and Rosa[24]
8	MT	MT	V5	Solomon and Rosa[24]
9	dlPFC	8Ad	A8aD	Liu et al.[1], Ji et al.[26]
10	PCC	7m	PGM	Liu et al.[1], Ji et al.[26]
11	PPC	PGi	LIP	Liu et al.[1], Ji et al.[26]

Supplementary references

1. Liu, C., Yen, C. C.-C., Szczupak, D., Ye, F. Q., Leopold, D. A., & Silva, A. C. Anatomical and functional investigation of the marmoset default mode network. Nat. Commun. **10**, 1–8 (2019).
2. Tian, X., Chen, Y., Majka, P., Szczupak, D., Perl, Y. S., Yen, C. C.-C., Tong, C., Song, K., Jiang, H., Glen, D., Rosa, M., Silva, A., Liang, Z., & Liu, C. An integrated resource for functional and structural connectivity of the marmoset brain. Nat. Commun. **13**, 7416 (2022).
3. Cox, R. W. AFNI: software for analysis and visualization of functional magnetic resonance neuroimages. Comput. biomed. res. **29**, 162-173 (1996).
4. Smith, S. M., Jenkinson, M., Woolrich, M. W., Beckmann, C. F., Behrens, T. E., Johansen-Berg, H. et al. Advances in functional and structural MR image analysis and implementation as FSL. Neuroimage **23**, S208-S219 (2004).
5. Paxinos, W.-C. P. M. R. M. T. H., G. The Marmoset Brain in Stereotaxic Coordinates. New York:Academic Press (2012).
6. Liu, C., Yen, C. C.-C., Szczupak, D., Tian, X., Glen, D., & Silva, A. C. Marmoset brain mapping v3: Population multi-modal standard volumetric and surface-based temeplates. Neuroimage ***226***, 117620 (2021).
7. Chung, F. Laplacians and the cheeger inequality for directed graphs. Ann. Comb. **9**, 1–19 (2005).
8. Chung, F. The diameter and laplacian eigenvalues of directed graphs. Electron. J. Comb. (pp. N4–N4) (2006).
9. Rubinov, M., & Sporns, O. Complex network measures of brain connectivity: uses and interpretations. Neuroimage **52**, 1059-1069 (2010).
10. Váša, F., & Mišić, B. Null models in network neuroscience. Nat. Rev. Neurosci. **23**, 493-504 (2022).
11. Preti, M. G., & Van De Ville, D. Decoupling of brain function from structure reveals regional behavioral specialization in humans. Nat. Commun. **10**, 1–7 (2019).
12. Huang, W., Bolton, T. A., Medaglia, J. D., Bassett, D. S., Ribeiro, A., & Van De Ville, D. A graph signal processing perspective on functional brain imaging. P. IEEE **106**, 868–885 (2018).
13. Margulies, D. S., Ghosh, S. S., Goulas, A., Falkiewicz, M., Huntenburg, J. M., Langs, G., Bezgin, G., Eickhoff, S. B., Castellanos, F. X., Petrides, M. et al. Situating the default-mode network along a principal gradient of macroscale cortical organization. Proc. Natl. Acad. Sci. U. S. A. **113**, 12574–12579 (2016).
14. Yang, S., Wagstyl, K., Meng, Y., Zhao, X., Li, J., Zhong, P., Li, B., Fan, Y.-S., Chen, H., & Liao, W. Cortical patterning of morphometric similarity gradient reveals diverged hierarchical organization in sensory-motor cortices. Cell Rep. **36**, 109582 (2021).
15. Meng, Y., Yang, S., Xiao, J., Lu, Y., Li, J., Chen, H., & Liao, W. Cortical gradient of a human functional similarity network captured by the geometry of cytoarchitectonic organization. Commun. Biol. **5**, 1152 (2022).
16. Alexander-Bloch, A. F., Shou, H., Liu, S., Satterthwaite, T. D., Glahn, D. C., Shinohara, R. T., Vandekar, S. N., & Raznahan, A. On testing for spatial correspondence between maps of human brain structure and function. Neuroimage **178**, 540–551 (2018).
17. V´aˇsa, F., Seidlitz, J., Romero-Garcia, R., Whitaker, K. J., Rosenthal, G., V´ertes, P. E., Shinn, M., Alexander-Bloch, A., Fonagy, P., Dolan, R. J. et al. Adolescent tuning of association cortex in human structural brain networks. Cereb. Cortex **28**, 281–294 (2018).
18. Wagner, H. H., & Dray, S. Generating spatially constrained null models for irregularly spaced data using m oran spectral randomization methods. Methods Ecol. Evol. **6**, 1169–1178 (2015).
19. Schwarzkopf, D. S., De Haas, B., & Rees, G. Better ways to improve standards in brain-

behavior correlation analysis. Front. Hum. Neurosci. **6**, 200 (2012).

20. Theodoni, P., Majka, P., Reser, D. H., W´ojcik, D. K., Rosa, M. G., & Wang, X.-J. Structural attributes and principles of the neocortical connectome in the marmoset monkey. Cereb. Cortex **32**, 15–28 (2022).
21. Atapour, N., Majka, P., Wolkowicz, I. H., Malamanova, D., Worthy, K. H., & Rosa, M. G. Neuronal distribution across the cerebral cortex of the marmoset monkey (callithrix jacchus). Cereb. Cortex **29**, 3836–3863 (2019).
22. Ngo, G. N., Hori, Y., Everling, S., & Menon, R. S. Joint-embeddings reveal functional differences in default-mode network architecture between marmosets and humans. NeuroImage **272**, 120035 (2023).
23. Glasser, M. F., Coalson, T. S., Robinson, E. C., Hacker, C. D., Harwell, J., Yacoub, E., Ugurbil, K., Andersson, J., Beckmann, C. F., Jenkinson, M. et al. A multi-modal parcellation of human cerebral cortex. Nature **536**, 171–178 (2016).
24. Solomon, S. G., & Rosa, M. G. A simpler primate brain: the visual system of the marmoset monkey. Front. Neural Circuits. **8**, 96 (2014).
25. Kaas, J. H. Evolution of somatosensory and motor cortex in primates. Anat. Rec. **281**, 1148-1156 (2004).
26. Ji, J. L., Spronk, M., Kulkarni, K., Repovš, G., Anticevic, A., & Cole, M. W. Mapping the human brain's cortical-subcortical functional network organization. Neuroimage **185**, 35-57 (2019).